inventions

MDPI

Article

Liquid Natural Gas Cold Energy Recovery for Integration of Sustainable District Cooling Systems: A Thermal Performance Analysis

Yang Luo [1,*], Xuesong Lu [2,3], Yi Chen [1], John Andresen [2] and Mercedes Maroto-Valer [2]

[1] School of Intelligent Manufacturing Ecosystem, Xi'an Jiaotong-Liverpool University, Suzhou 215123, China; yi.chen02@xjtlu.edu.cn
[2] Research Centre for Carbon Solutions, School of Engineering and Physical Sciences, Heriot-Watt University, Edinburgh EH14 4AS, UK; xuesong.lu@eng.ox.ac.uk (X.L.); j.andresen@hw.ac.uk (J.A.); m.maroto-valer@hw.ac.uk (M.M.-V.)
[3] Department of Engineering Science, University of Oxford, Oxford OX1 3PJ, UK
* Correspondence: yang.luo@xjtlu.edu.cn

Abstract: This paper investigates the heat transfer properties of liquefied natural gas (LNG) in a corrugated plate heat exchanger and explores its application in cold energy recovery for enhanced energy efficiency. The study aims to integrate this technology into a 500 MW gas-fired power plant and a district cooling system to contribute to sustainable city development. Using computational fluid dynamics simulations and experimental validation, the heat transfer behaviour of LNG in the corrugated plate heat exchanger is examined, emphasising the significance of the gas film on the channel wall for efficient heat transfer between LNG and water/ethylene glycol. The study analyses heat exchange characteristics below and above the critical point of LNG. Below the critical point, the LNG behaves as an incompressible fluid, whereas above the critical point, the compressible supercritical state enables a substantial energy recovery and temperature rise at the outlet, highlighting the potential for cold energy recovery. The results demonstrate the effectiveness of cold energy recovery above the critical point, leading to significant energy savings and improved efficiency compared to conventional systems. Optimal operational parameters, such as the number of channels and flow rate ratios, are identified for successful cold energy recovery. This research provides valuable insights for sustainable city planning and the transition towards low-carbon energy systems, contributing to the overall goal of creating environmentally friendly and resilient urban environments.

Keywords: cold energy recovery; liquefied natural gas (LNG); corrugated plate heat exchanger; sustainable cooling; numerical simulation; district cooling system (DCS)

Citation: Luo, Y.; Lu, X.; Chen, Y.; Andresen, J.; Maroto-Valer, M. Liquid Natural Gas Cold Energy Recovery for Integration of Sustainable District Cooling Systems: A Thermal Performance Analysis. *Inventions* **2023**, *8*, 121. https://doi.org/10.3390/inventions8050121

Academic Editor: Alessandro Dell'Era

Received: 7 August 2023
Revised: 13 September 2023
Accepted: 19 September 2023
Published: 25 September 2023

1. Introduction

Space cooling in buildings has become a significant concern due to the growing global trend of seeking greater comfort through increased energy usage. Conventional cooling methods, such as air conditioning units, often contribute to high energy consumption [1,2] and significant greenhouse gas emissions [3]. These methods rely on refrigerants that have potent global warming potential [4], further exacerbating the climate crisis. The energy-intensive nature of traditional cooling practices strains energy resources and contributes to increased carbon dioxide emissions. In Southeast Asia, where high temperatures and humidity levels prevail, the electricity consumption for cooling in buildings showed a significant surge, increasing approximately 7.5 times between 1990 and 2017, from 10 TWh to almost 75 TWh [5]. In the coming decades, the region is projected to witness a significant increase in electricity usage attributed to cooling, which is anticipated to rise from a mere 8% in 2017 to nearly 19%. Moreover, during periods of peak demand, it is expected to escalate to around 30% [6]. This upswing in cooling requirements during

peak periods poses a potential challenge to the region's power infrastructure and presents an opportunity to develop an alternative cooling supply. Considering these challenges, the focus on sustainable cooling solutions has become imperative for global communities. Among the various approaches being explored, district cooling systems (DCS) have gained considerable attention from industry and academia.

DCS has emerged as a crucial technology because it provides high-quality cooling and high efficiency. This system finds significant applications in areas with a high concentration of buildings. With a district cooling system, thermal energy is generated centrally and distributed to various customers, including commercial, residential, institutional, and industrial sectors. The energy supplied by the DCS is primarily utilised for space cooling and dehumidification purposes. Traditional DCS energy sources rely heavily on vapour compression refrigeration powered by fossil fuel-generated electricity. These systems often remain underutilised due to suboptimal designs, operational practices, and financial considerations [7]. In recent studies focusing on DCS in regions with high cooling demand, researchers have concentrated on enhancing the sustainability of these systems. One key area of improvement identified in a recent review by [8] is the replacement of fossil fuel-driven compression chillers with more environmentally friendly alternatives. These alternatives include absorption refrigeration systems powered by renewable energy sources like solar or biomass and compression chillers driven by renewable electricity. Alongside these changes, key research focuses have been to optimise chiller capacity, incorporate thermal energy storage, reduce exergy losses in chilled water distribution networks, implement advanced control strategies, and refine modelling and optimisation methodologies. These efforts collectively aim to maximise the efficiency and sustainability of district cooling systems. Another area of interest is the utilisation of low-grade renewable thermal energy, characterised by temperatures of 250 °C or lower, sourced from various sustainable options such as solar collectors [9,10], geothermal energy [11,12], seawater [13,14], and waste heat sources [15]. The potential for harnessing waste cold and effectively integrating DCS with other sectors, such as power generation and space cooling, within a comprehensive, innovative energy system approach remains relatively unexplored.

The recovery of cold energy from liquefied natural gas (LNG) regasification processes has garnered significant attention in recent years to minimise cooling energy consumption and greenhouse gas emissions. From 2020 to 2021, there was a 4.5% increase in the global LNG trade, which reached 372.3 million metric tons (MT). As of April 2022, the total global regasification capacity stood at 901.9 million tones per annum (MTPA) spread across 40 markets [16], which is equivalent to a cold energy of 7.485×10^{14} kJ per year. These facilities are notably present in hot and/or sub-tropical regions such as India, Latin America, the Middle East, and Southeast Asia [16]. Simultaneously, floating storage and regasification units (FSRUs) are increasing due to their flexibility and economic advantages compared to onshore units. In the regasification process, the cold energy stored in LNG is released when it is converted from its liquid state at approximately −162 °C to a gaseous phase at around 25 °C. This cold energy is typically dissipated into the surrounding environment, specifically through the use of LNG vaporisers. These vaporisers, such as Open Rack Vaporizers (ORV) [17,18], Submerged Combustion Vaporizers (SCV) [19,20], and Intermediate Fluid Vaporizers (IFV) [21], facilitate the phase change of LNG. The released cold energy is transferred to a heat transfer medium, often seawater, which absorbs the heat and facilitates the conversion of LNG into its gaseous form (Figure 1). This process leads to the wastage of exergy, including seawater pumping work and cold, and causing marine pollution [22]. Approximately 350 kJ/kg_{LNG} of waste exergy is dissipated to the environment during LNG regasification at typical natural gas distribution pressures, with no recovery [23].

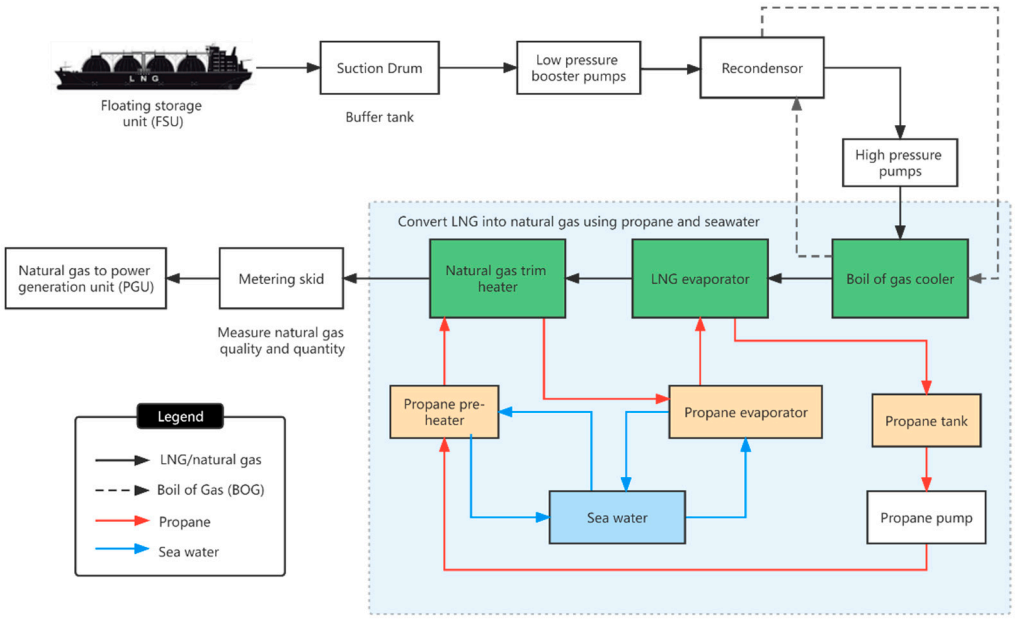

Figure 1. Simplified flow overview of LNG gasification plant.

The utilisation of LNG cold energy for direct cooling applications has been relatively understudied in academic literature. It is proposed by [24] that a polygeneration plant utilise LNG-regasification cold recovery to generate power and provide cold through a district cooling network by using CO_2 as a Rankine working fluid and cold-carrying medium. It achieves significant energy savings of 81.1 kW h/ton-LNG with an exergetic efficiency of 34.7%, while also reducing seawater consumption by 67.6% compared to typical LNG regasification processes. Dominkovi [25] carried out a case study with scenario-based modelling on the district cooling grid to analyse the potential of future DCSs in Singapore. The proposed model achieves a 19.5% reduction in primary energy demand, a 38.4% decrease in socio-economic costs, and a 41.5% reduction in CO_2 emissions compared to the business-as-usual scenario. Sermsuk [26] studied the feasibility of integrating an LNG receiving terminal with a data centre, utilising a combination of Rankine cycle and direct expansion cycle. The system can produce a significant amount of cold water (44.23 MW) at 7 °C, sufficient to cool a data centre with 5345 racks, resulting in a reduction of 13,521 kWh in cooling and 83,859 tons of annual CO_2 emissions. Considering these individual studies and the projected growth of the global LNG regasification capacity, particularly in cooling-dominated regions, the recovery of LNG cold energy holds the potential to enhance the sustainability of DCSs in LNG importing zones [16]. The majority of existing research on the utilisation of LNG cold exergy has predominantly concentrated on exploring its potential applications. However, a limited body of literature specifically examines the direct cold recovery and the associated thermodynamic performance aspects of this process. The knowledge gap is the integration of LNG cold energy recovery and district cooling systems and the feasibility of LNG cold energy recovery by corrugated plate heat exchanger for district cooling systems.

Hence, the proposed study investigates the technical feasibility of integrating space cooling via DCS and LNG regasification systems through direct cold recovery with corrugated plate heat exchangers. Lab-based experimental study and simulation are conducted to simulate the cold exergy recovery potential from LNG used in a DCS in combination with a 500 MW gas-fired power plant. The novelties include (1) the identification of a film formation that restricts cold energy recovery, (2) the suggestion that LNG cold energy recovery should occur within the supercritical phase to avoid film formation, and (3) the demonstration of the viability of LNG cold recovery for district cooling systems. The outcomes of this study could serve as a reference for implementing LNG cold energy recovery in district cooling systems.

2. Methodology

The research methodology encompasses several key steps, and the process flow diagram is shown in Figure 2. Initially, an experimental setup was designed and implemented to validate the simulation models. This involved using a liquid nitrogen (LN)–water system to replicate the heat transfer conditions within the corrugated plate heat exchanger. Following this, 2D simulation models were developed using COMSOL software, incorporating the turbulent flow module with the k-ω model to simulate fluid flow and the heat transfer module to predict heat flux and outlet temperatures. The velocity field and the formation of a gas film were analysed through simulation runs, investigating their impact on heat transfer.

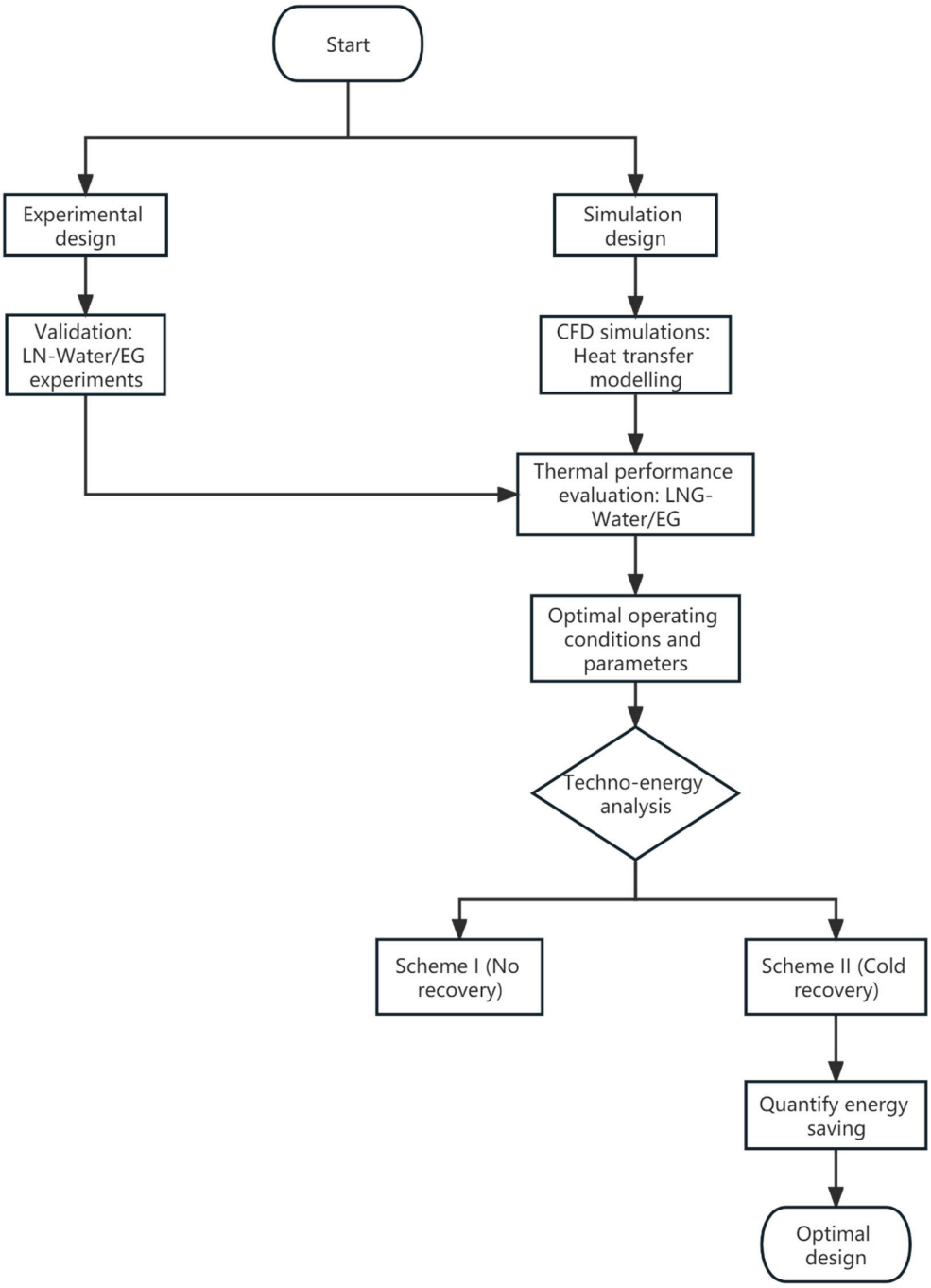

Figure 2. Process flow diagram for the streamlined design of empirical and simulation study.

Furthermore, the simulation results were validated by comparing them with experimental data, mainly focusing on the water outlet temperatures. The heat exchange behaviour between LNG and water/ethylene glycol (EG) was assessed by examining the methane phase diagram, considering different pressure conditions below and above the critical point. The heat exchange performance of LNG and water/EG below the critical point was evaluated by analysing factors such as mass flow rates, temperature variations, and mass flow rate ratios. A comparison was then made between the heat exchange characteristics of LNG and water/EG below and above the critical point, focusing on velocity and temperature distributions to identify optimal operating conditions for efficient heat transfer.

Finally, to evaluate the feasibility of the proposed system, a techno-energy analysis was carried out by assessing a natural gas-fired power plant and a district cooling system, both with and without integrating an LNG cold energy recovery system.

2.1. Experimental Method

As shown in Figure 3, the experimental configuration utilised LN as the cryogenic medium and water/EG as the thermal medium, operating at a pressure of 20 bar. The initial temperatures of LN and water were recorded as 77.4 Kelvin (K) and 323.2 K, respectively. The ratio of the mass flow rate of LN to water was 3:1. The distinguishing feature of this heat exchanger lies in its curved corrugated bends, which effectively augment the process of heat transfer. Figure 4a provides an illustration of the comprehensive visual representation of the heat exchanger plate, while Figure 4b displays the internal configuration of the plate as depicted through a computed tomography (CT) image. Table 1 presents a concise overview of the dimensional and structural parameters pertaining to a corrugated heat exchanger. The heat exchanger's aspect ratio is calculated using Equation (1), while the surface enlargement factor is determined through Equation (2).

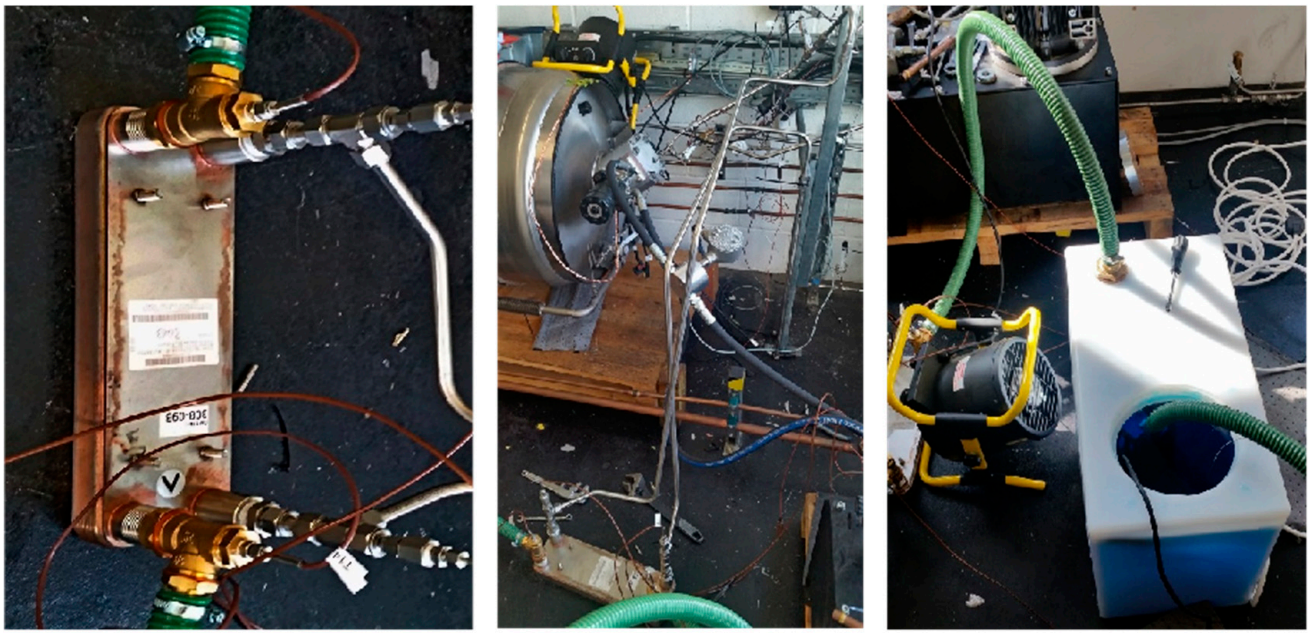

Figure 3. Experimental setup for thermal performance testing of the corrugated plate heat exchanger with LN–water/EG heat transfer.

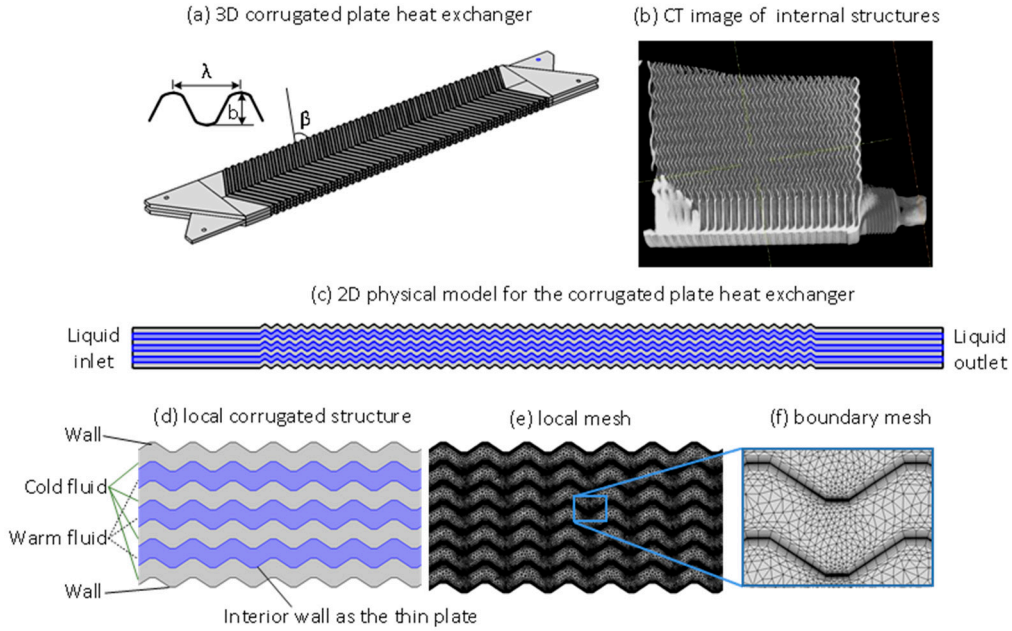

Figure 4. The corrugated plate heat exchanger, 2D physical model and meshes.

Table 1. Dimension and parameters of the corrugated plate heat exchanger.

Parameter	Value	Parameter	Value
Length of exchanger (mm)	322	Width of exchanger (mm)	76
Number of channels	15/15	Thickness of plate (mm)	0.385
Width of channel (mm)	3.37	Chevron angle, β (°)	60
Corrugation depth, b (mm)	1.66	Corrugation wavelength, λ (mm)	7.00
Aspect ratio, γ	0.47	Surface enlargement factor, η	1.13

The equation for aspect ratio:

$$\gamma = \frac{2b}{\lambda} \tag{1}$$

where γ is the aspect ratio of chevron corrugation; λ is the corrugation pitch; b is the corrugation amplitude.

$$\eta = \frac{1}{6}\left[1 + \sqrt{1 + \left(\frac{\pi\gamma}{2}\right)^2} + 4 \times \sqrt{1 + 0.5\left(\frac{\pi\gamma}{2}\right)^2}\right] \tag{2}$$

where η is the enlargement factor of the corrugation surface.

2.2. Simulation Method

COMSOL 5.2a was utilised for conducting simulations of heat transfer and fluid flow in the corrugated plate heat exchanger. Specifically, the turbulent flow module and the heat transfer module for fluid were employed in the simulations. Two different systems were considered: the LN–water/EG mixture and the LNG–water/EG mixture. These systems were chosen to assess the fluid flow characteristics and thermal performance within the corrugated plate heat exchanger. For the LNG system, simulations were performed both below and above the critical point of the material. The properties of the substances involved and the operational parameter settings can be found in Table 2.

Table 2. Properties of materials and operational conditions.

System 1 (Liquid Nitrogen (LN)–Water)		
Parameter	LN	Water
Density (kg/m^3)	808.5	1000
Viscosity (Pa·s)	1.58×10^{-4}	8.9×10^{-4}
Thermal conductivity (W/(m·K))	0.135	0.615
Heat capacity (J/(kg·K))	2024	4186
Temperature inlet (K)	77.4 (−195.8 °C)	323.2 (50 °C)
Pressure (bar)	20	1
Mass flow rate (kg/s)	0.005, 0.010, 0.164	0.015, 0.030, 0.492
Ratio of mass flow rate	1:3	3:1
Thickness of gas film (mm)	0.2	
Thermal conductivity of gas film (W/(m·K))	0.007	
System 2 (Liquefied natural gas (LNG)–water/ethylene glycol (EG)) Under critical pressure, e.g., (10 bar)		
Parameter	LNG	Water/EG
Density (kg/m^3)	468	1031
Viscosity (Pa·s)	1.03×10^{-4}	0.0035
Thermal conductivity (W/(m·K))	0.2	0.5011
Heat capacity (J/(kg·K))	3504	3784
Temperature inlet (K)	111.2 (−162 °C)	303.2 (30 °C)
Pressure (bar)	10	1
Mass flow rate (kg/s)	0.005, 0.010, 0.164	0.015, 0.030, 0.492
Ratio of mass flow rate	1:3	3:1
Thickness of gas film (mm)	0.2	
Thermal conductivity of gas film (W/(m·K))	0.011	
System 3 (Liquefied natural gas (LNG)–water/ethylene glycol (EG)) Above critical pressure, e.g., (70–100 bar)		
Parameter	LNG	Water/EG
Density (kg/m^3)	ρ (Table 3)	1031
Viscosity (Pa·s)	μ (Table 3)	0.0035
Thermal conductivity (W/(m·K))	k (Table 3)	0.5011
Heat capacity (J/(kg·K))	C_p (Table 3)	3784
Temperature inlet (K)	111.2 (−162 °C)	303.2 (30 °C)
Pressure (bar)	70–100	1
Mass flow rate (kg/s)	0.005	0.025
Ratio of mass flow rate	1:5	5:1

Table 3. Nature gas (NG) properties of supercritical state at 70–100 bar [27].

Temperature (K)	**Density (kg/m^3)**
111–223	$\rho = -2.45869 + 15.12763 \times T - 0.16537 \times T^2 + 7.459 \times 10^{-4} \times T^3 - 1.29548 \times 10^{-6} \times T^4$
223–271	$\rho = 11091.66885 - 119.03258 \times T + 0.43352 \times T^2 - 5.30962 \times 10^{-4} \times T^3$
271–385	$\rho = 2634.06161 - 26.70158 \times T + 0.10675 \times T^2 - 1.93454 \times 10^{-4} \times T^3 + 1.32923 \times 10^{-7} \times T^4$

Table 3. *Cont.*

Temperature (K)	Viscosity (Pa·s)
111–218	$\mu = 8.02631 \times 10^{-4} - 1.01809 \times 10^{-5} \times T + 4.71489 \times 10^{-8} \times T^2 - 7.71822 \times 10^{-11} \times T^3$
218–254	$\mu = 4.64105 \times 10^{-4} - 3.52808 \times 10^{-6} \times T + 6.9276 \times 10^{-9} \times T^2$
254–385	$\mu = 9.67009 \times 10^{-5} - 7.43585 \times 10^{-7} \times T + 2.1834 \times 10^{-9} \times T^2 - 2.07823 \times 10^{-12} \times T^3$
Temperature (K)	Thermal conductivity (W/(m·K))
111–235	$k = 0.30675 - 6.44568 \times 10^{-4} \times T - 4.35253 \times 10^{-6} \times T^2 + 1.07039 \times 10^{-8} \times T^3$
235–262	$k = 0.62882 - 0.00432 \times T + 7.96913 \times 10^{-6} \times T^2$
262–385	$k = 0.33402 - 0.00258 \times 10^{-2} \times T + 7.36829 \times 10^{-6} \times T^2 - 6.69403 \times 10^{-9} \times T^3$
Temperature (K)	Heat capacity (J/(kg·K))
111–223	$C_p = -9567.33957 + 263.05475 \times T - 1.83425 \times T^2 + 0.00436 \times T^3$
223–261	$C_p = -892240.75366 + 11278.86482 \times T - 46.88971 \times T^2 + 0.06448 \times T^3$
261–385	$C_p = 53206.50774 - 423.72673 \times T + 1.18621 \times T^2 - 0.00111 \times T^3$

2.2.1. Governing Equations

The mass equation is

$$\nabla \cdot (\rho u) = 0 \tag{3}$$

where ρ is the density; u is the velocity.

The momentum equation is

$$\rho(u \cdot \nabla)u = \nabla \cdot \left[-p + (\mu + \mu_T)\left(\nabla u + (\nabla u)^T \right) \right] \tag{4}$$

where p is the pressure; μ is the dynamic viscosity; μ_T is the turbulent viscosity. The k-ω turbulence model was used to obtain μ_T.

The energy equation is

$$\rho C_p (u \cdot \nabla)T = -(\nabla \cdot q) + \tau : S - \frac{T}{\rho}\frac{\partial \rho}{\partial T} \cdot (u \cdot \nabla)p + Q \tag{5}$$

where C_p is heat capacity; T is temperature; q is heat flux; τ is stress tensor; S is strain rate tensor; Q is heat source.

2.2.2. Simulation Method

A two-dimensional (2D) physical model, depicted in Figure 4c, was constructed for the purpose of conducting computational fluid dynamics (CFD) simulations, similar to the approach described in the referenced literature [28]. In this model, the dark grey channels (numbered 1, 3, 5, 7 from the bottom) represent the passages for the cold fluid, which can be either LN or LNG, while the blue channels (numbered 2, 4, 6 from the bottom) represent the passages for the warm fluid, which can be either water or a water/EG mixture. The fluid flows from the left side to the right side of the model. The inner wall is represented as a thin layer plate, as illustrated in Figure 4d. The meshing of the model is demonstrated in Figure 4e, consisting of a total of 268,412 grids. A boundary layer with eight layers of mesh is applied to the wall area, as depicted in Figure 4f.

The assumptions made for numerical investigations are as follows: (i) The properties of materials, such as density and viscosity, remain constant when the temperature varies below the critical point. This assumption is based on the observation that the temperature variations are relatively small, less than 20 K. (ii) The material properties, on the other hand, do change with temperature above the critical point, as indicated in Table 3. (iii) It is assumed that each channel with single-phase liquid flow does not undergo phase changes, such as from liquid to solid or from liquid to gas. This assumption is supported by experiments conducted without any observed phase changes. (iv) Finally, it is assumed that both the flow and heat transfer processes are in a steady state.

3. Validation of Models with Liquid Nitrogen (LN)–Water System

3.1. Velocity Field

The validation experiment and simulation were performed utilising a system comprising LN and water. In order to obtain a deeper understanding of the fluid dynamics occurring within the corrugated plate, a computational simulation was conducted to visually depict the velocity distribution. The simulation encompassed a water mass flow rate of 0.164 kg/s and a LN mass flow rate of 0.492 kg/s. The water was initially introduced into the system with a temperature of 323.2 K, whereas the LN entered the system at a temperature of 77 K. Figure 5a depicts the velocity field, indicating that the central regions of the channels exhibit the highest velocities.

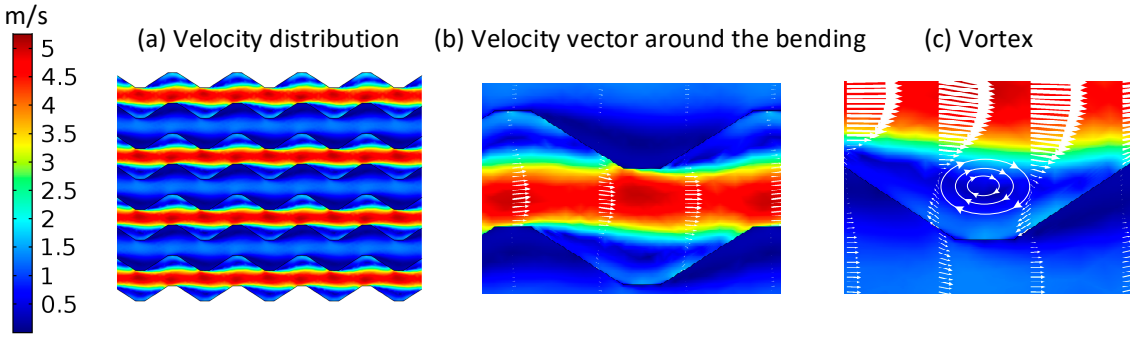

Figure 5. Velocity vector field of the corrugated plate heat exchanger (U_{water} = 0.164 kg/s; U_{LN} = 0.492 kg/s; T_{in_water} = 323.2 K; T_{in_LN} = 77.4 K).

Furthermore, the velocities exhibit relatively higher values at the upper and lower walls of the bends compared to the adjacent layer. Figure 5b presents an expanded depiction of the fluid flow in the local region, revealing the presence of a clearly defined vortex surrounding the curved bending area, as illustrated in Figure 5c. The presence of these vortices leads to heightened velocities in the vicinity of the upper and lower walls of the bends, consequently augmenting heat transfer by facilitating the renewal of the boundary layer through the process of back mixing. The water system functions under a pressure of approximately 1.0×10^4 Pa, whereas the LN encounters a pressure decrease of 1.0×10^5 Pa.

3.2. Effect of Gas Film

The simulation results revealed the presence of a thin gas film adhering to the plate, which was validated by comparing it with experimental values. The gas film has a thickness of approximately 0.2 mm and plays a crucial role in heat transfer. The top diagram of Figure 6a illustrates the location of this gas film. Conversely, when the gas film is absent, as depicted in the top diagram of Figure 6b, the outlet temperature of water deviates significantly from the expected values, as shown in Figure 6. The conditions for this scenario include a water flow rate of 0.005 kg/s, a water inlet temperature of 323.2 K, an LN inlet temperature of 77.4 K, and an LN flow rate of 0.015 kg/s. In the presence of the gas film, the water outlet temperature is 293.2 K, aligning closely with the experimental data (Figure 6a). However, without the gas film, the water outlet temperature drops to approximately 168.2 K, as depicted in Figure 6b, diverging from the actual observations. This discrepancy underscores the critical role of the gas film in mediating heat transfer between LN and water. The mechanism responsible for the formation of the gas film along the plate wall is yet to be fully understood. Possible explanations include (i) rapid vaporisation of LN upon initial heat transfer with water, leading to the formation of a gas film that impedes further heat transfer, and (ii) the formation of a gas film along the wall to maintain vapour equilibrium pressure. The precise factors influencing gas film formation warrant further investigation through experiments and simulations.

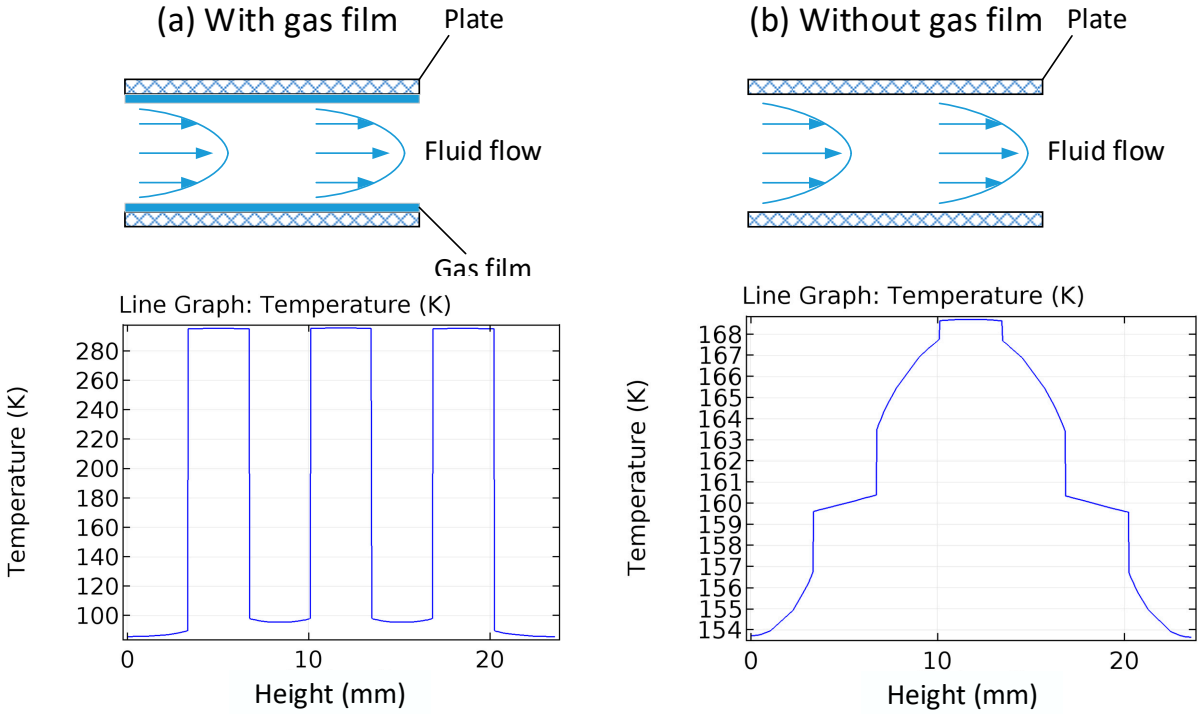

Figure 6. Comparison of heat transfer between with gas film (**a**) and without gas film (**b**) (U_{water} = 0.005 kg/s; U_{LN} = 0.015 kg/s; T_{in_water} = 323.2 K; T_{in_LN} = 77.4 K).

3.3. Model Validation by the Experiments

The simulation results for the 2D models were validated against experimental data. The comparison of predicted and experimental water outlet temperatures is presented in Table 4. The experimental water temperatures for three different water velocities, namely 0.02 m/s, 0.04 m/s, and 0.64 m/s, were found to be 294.2 K, 307.7 K, and 321.9 K, respectively. The simulation predicted water temperatures of 295.2 K, 308.3 K, and 322.1 K, respectively, resulting in an error of only 2.3%. This comparison demonstrates the efficacy of the current models in accurately predicting the water outlet temperatures.

Table 4. Validation of simulation models by the experimental data.

Exp. No.	m_{LN} (kg/s)	m_{water} (kg/s)	u_{LN} (m/s)	u_{water} (m/s)	Re_{LN}	Re_{water}	$T_{waterexp}$ (K)	$T_{waterSim}$ (K)
1	0.015	0.005	0.074	0.020	1276	76	294.2	295.2
2	0.030	0.010	0.149	0.040	2569	151	307.7	308.3
3	0.492	0.164	2.377	0.641	40,990	2427	321.9	322.1

In summary, the CFD models successfully simulated the heat transfer between LN and water in the plate heat exchanger. The chosen model and simulation settings for fluid flow and heat transfer were appropriate and aligned with the corrugated plate heat exchanger simulation. The simulation results highlighted the significance of the gas film in facilitating heat transfer, particularly when LN operation is below the critical pressure point. Moving forward, the validated models will be expanded to include the application of LNG water/EG mixture systems.

4. Results and Discussions

4.1. Gas Phase Diagram and Heat Exchange Performance

The phase diagram of methane is depicted in Figure 7, revealing its critical point at 46 bar and 190.6 K. Below this critical point, there exists a distinct phase change boundary

between the liquid and gas phases, requiring separate treatment for each phase. Conversely, above the critical point, there is no discernible demarcation between the compressible liquid and supercritical state. The liquid and supercritical phases can be regarded as a single compressible phase. Consequently, LNG heat transfer entails two distinct operations: one below the critical point and another above it. Below the critical point, the material properties of the liquid and gas phases can be assumed to be constant. However, above the critical point, the density, viscosity, heat capacity, and thermal conductivity undergo significant changes with varying temperatures and pressures. In such cases, a gas film does not form in the heat exchanger, as demonstrated in the literature [27]. The heat exchange performance between LNG and water/EG exhibits notable differences under these conditions. Subsequent sections will delve into analysing heat transfer behaviour between LNG and water/EG in the corrugated plate heat exchanger through simulations.

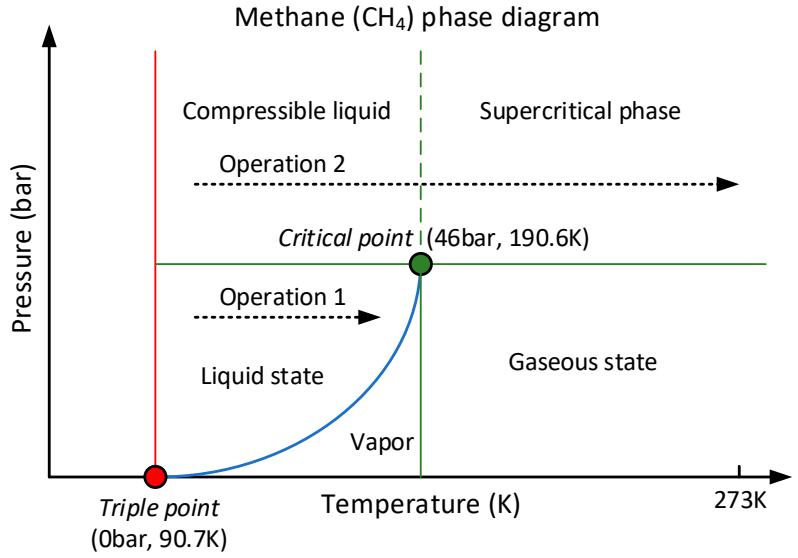

Figure 7. Methane phase diagram.

4.2. Heat Exchange between LNG and Water/EG below Critical Point

The physical properties of natural gas (NG), including density, viscosity, heat capacity, and thermal conductivity, display minor fluctuations when subjected to varying temperatures and pressures in its liquid state below the critical point. Consequently, LNG has the ability to be regarded as a fluid that is incompressible when utilised in the context of a corrugated plate heat exchanger.

Expanding on the findings presented in Section 4, our study delves into examining LNG and water/EG systems under an LNG pressure of 10 bar. The proportion of water to EG in terms of volume is established as 7:3, resulting in a freezing point of 259.2 K for the water/EG mixture. The present system maintains a constant temperature of 111.2 K for the LNG inlet, whereas the inlet temperature for water/EG can vary between 293.2 K and 303.2 K. The thickness of the gas film is observed to be 0.2 mm, while the ratio of the mass flow rate of LNG to water/EG is 3:1.

The graphical representation depicted in Figure 8a demonstrates the correlation between the Reynolds number of water/EG and the outlet temperature of water/EG. The results indicate a clear correlation between the increase in water/EG Reynolds number, ranging from 20 to 620, and a subsequent rise in the water/EG outlet temperature, which ranges from 267.0 K to 301.8 K. These observations were made under the condition that the water/EG inlet temperature remained constant at 303.2 K. Moreover, elevating the inlet temperature of the water/ethylene glycol mixture from 293.2 K to 303.2 K results in a rise of about 10 K in the outlet temperature of the same mixture. On the other hand, it can be observed from Figure 8b that as the Reynolds number of LNG increases from 1960 to 62,890, there is a corresponding decrease in the outlet temperature of LNG from 124.7 K to

111.7 K. The present scenario involves the utilisation of a high mass flow rate of LNG to prevent the freezing of water/EG in the heat exchanger.

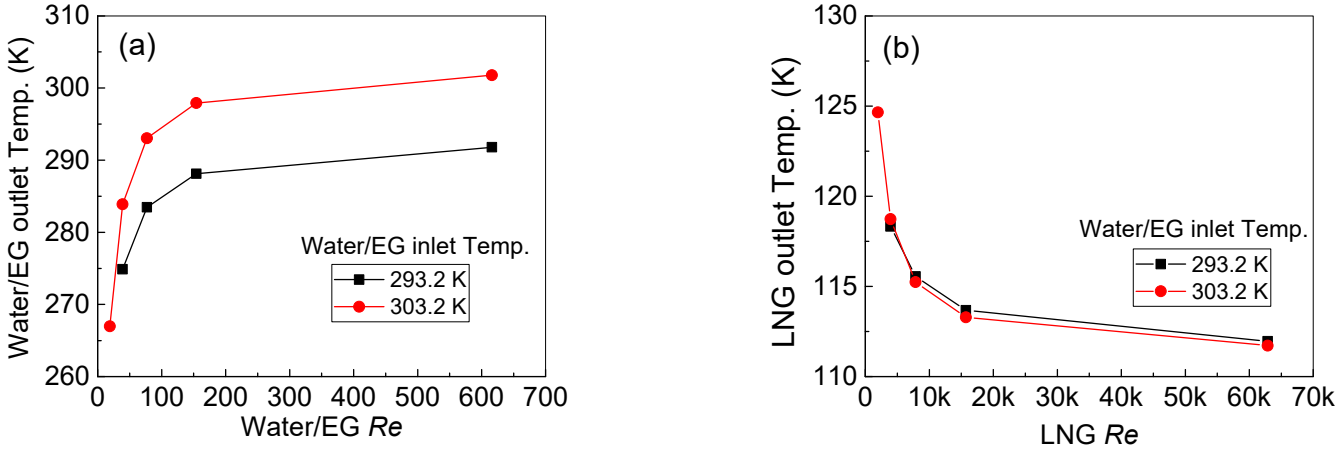

Figure 8. Relationship between Re and outlet temperature at 10 bar (**a**) water/EG; and (**b**) LNG.

Conversely, a low mass flow rate of water/EG is employed to prevent the partial gasification of LNG in the heat exchanger. However, owing to the constraints imposed by the gas film and the alteration of the water/EG and LNG phases in the heat exchanger, the temperature of the LNG outlet undergoes a moderate rise of 20–30 K compared to the temperature of the LNG inlet. Considering the conventional mass flow rate ratio of LNG to water/EG, which is 3:1, the efficacy of heat transfer between LNG and water/EG may not be the most favourable option when LNG is in its incompressible liquid state.

4.3. Comparison of Heat Exchange between LNG and Water/EG below and above the Critical Point

Apart from the heat transfer of LNG in the incompressible liquid phase, which occurs at a pressure of 10 bar (Operation 1 in Figure 7), the thermal interaction between LNG and water/EG also be carried out beyond the critical point of natural gas, specifically at a pressure range of 70–100 bar (Operation 2 in Figure 7).

The velocity distribution in a corrugated plate heat exchanger is compared between LNG's incompressible liquid and compressible fluid states in Figure 9a,b. At the state of being an incompressible liquid, the flow rates of mass for LNG and water/EG are 0.03 kg/s and 0.01 kg/s, respectively. The inlet temperatures for LNG and water/EG are established at 111.2 K and 303.2 K, respectively. The velocity distribution of LNG in each channel is depicted in Figure 9a, exhibiting uniformity along the x and z axes and at the outlet. Conversely, when in a state of compressible fluid, and with a flow rate of 0.005 kg/s for LNG and 0.025 kg/s for water/EG, along with identical inlet temperatures as previously stated, Figure 9b illustrates a non-uniform velocity distribution of NG within the heat exchanger. The velocity of NG exhibits an increment in the *x*-axis direction, with relatively greater velocities observed in the central channels as compared to the velocities observed on the remaining two sides. The anomalous velocity distribution observed in the heat exchanger is ascribed to the fluctuations in density and viscosity that occur as a function of temperature.

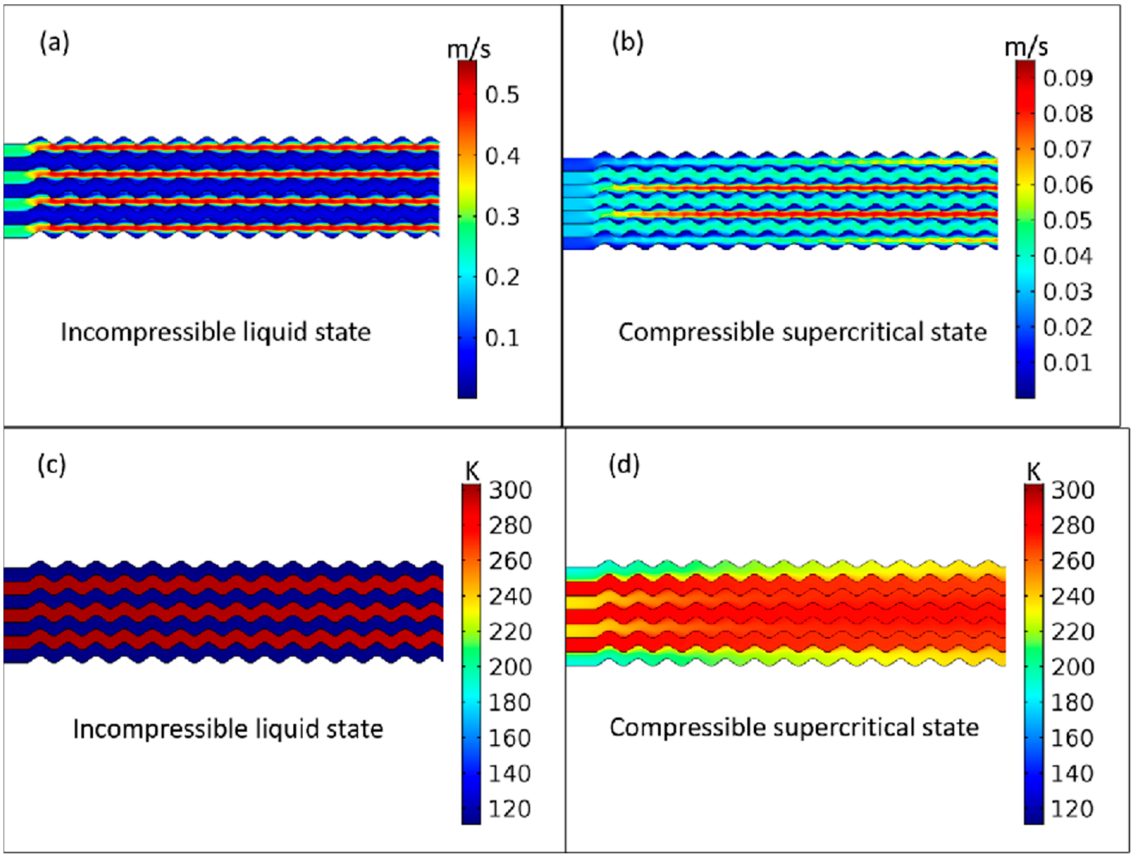

Figure 9. Comparison of LNG heat transfer between incompressible liquid state (**a**,**c**) ($U_{water/EG}$ = 0.01 kg/s; U_{LNG} = 0.03 kg/s; $T_{in\_water/EG}$ = 303.2 K; T_{in_LNG} = 111.2 K) and compressible supercritical state (**b**,**c**) ($U_{water/EG}$ = 0.025 kg/s; U_{LNG} = 0.005 kg/s; $T_{in\_water/EG}$ = 303.2 K; T_{in_LNG} = 111.2 K). Velocity: (**a**,**b**); temperature distribution: (**c**,**d**).

The temperature distribution between the incompressible liquid state of LNG and the compressible fluid state is illustrated in Figure 9c,d for the corrugated plate heat exchanger. In the context of incompressible liquids, the existence of a gaseous film serves to impede the transfer of heat from water/EG to LNG, thereby causing a limited degree of temperature dispersion in the x and z dimensions of the LNG. The temperature at the outlet exhibits a high degree of consistency across all channels. On the other hand, it can be observed that in the state of compressible fluid, the temperature of the NG experiences significant variations in both the x and z axes. In the context of incompressible liquids, the customary ratio of mass flow rates between LNG and water/EG is 3:1, while the outlet temperature of LNG falls within the range of 115 K to 125 K. In the state of compressible fluid, the customary ratio of the mass flow rate of LNG to water/EG is 1:5, and the temperature of the NG outlet can attain 270 K to 280 K. It can be inferred that the recuperation of low-temperature energy from the LNG ought to be carried out in the compressible fluid phase.

4.4. Effect of Influencing Parameters on Heat Exchange between LNG and Water/EG above NG Critical Point

This section presents an analysis of the impact of different parameters, such as the number of channels, inlet temperature of water/EG, and mass flow rates of water/EG and LNG, on the NG outlet temperature while maintaining an LNG pressure of 70 bar. Figure 10 illustrates the outcomes of the simulation. The LNG inlet temperature is consistently established at 111.2 K across all instances. The NG outlet temperatures for varying numbers of channels are depicted in Figure 10a, with a constant mass flow rate of 0.005 kg/s for LNG and 0.025 kg/s for water/EG. The inlet temperature for the water/EG mixture is 303.2 Kelvin. The findings indicate that the maximum temperature is situated at the

centre of the heat exchanger, whereas the minimum temperatures are located in close proximity to the walls on either side. Upon increasing the number of channels from 5 to 11, a noticeable alteration in the temperature distribution is observed. Specifically, the temperature distribution transforms from a relatively uniform curve, centred around 267.2 K–267.6 K, to a steep, sharply parabolic curve. The latter curve exhibits a maximum temperature of 272.1 K and a minimum temperature of 262.1 K.

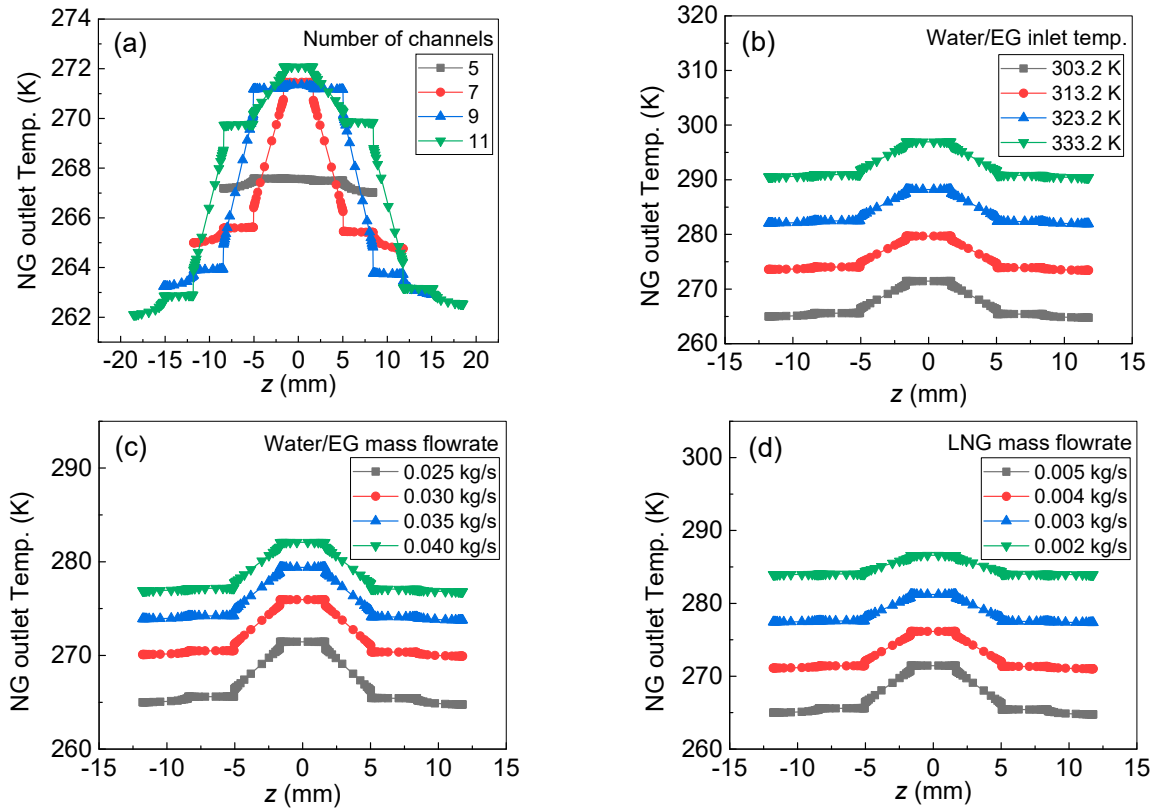

Figure 10. Effect of channel number (**a**), water/EG temperature (**b**), water mass flowrate (**c**) and LNG mass flow rate (**d**) on the NG outlet temperature. Conditions for (**a**): $U_{water/EG}$ = 0.025 kg/s; U_{LNG} = 0.005 kg/s; $T_{in\_water/EG}$ = 303.2 K; T_{in_LNG} = 111.2 K; for (**b**): $U_{water/EG}$ = 0.0025 kg/s; T_{in_LNG} = 111.2 K; for (**c**): U_{LNG} = 0.005 kg/s; $T_{in\_water/EG}$ = 303.2 K; T_{in_LNG} = 111.2 K; for (**d**): $U_{water/EG}$ = 0.025 kg/s; U_{LNG} = 0.005 kg/s; $T_{in\_water/EG}$ = 303.2 K.

The NG outlet temperature for varying water/EG inlet temperatures is depicted in Figure 10b, with a constant mass flow rate of 0.005 kg/s for LNG and 0.025 kg/s for water/EG. The increase in water/EG inlet temperature from 303.2 K to 333.2 K is observed to cause a corresponding rise in the NG outlet temperature from 265.0 K–271.5 K to 290.5 K–296.9 K. Figure 10c depicts the NG outlet temperature as a function of the water/EG mass flow rate, which ranges from 0.025 kg/s to 0.040 kg/s, while the LNG mass flow rate remains fixed at 0.005 kg/s. The water/EG inlet temperature is held constant at 303.2 K. The mass flow rate ratios for water/EG to LNG are 5, 6, 7, and 8. The findings of the study suggest that with an increase in the mass flow rate of water/EG, the NG outlet temperature rises from the initial range of 265.0 K–271.5 K to 276.9 K–282.1 K and eventually reaches the upper limit temperature of 303.2 K, which is the temperature of water/EG. The NG outlet temperature is depicted in Figure 10d as a function of the LNG mass flow rate, ranging from 0.002 kg/s to 0.005 kg/s while maintaining a constant water/EG mass flow rate of 0.025 kg/s and a water/EG inlet temperature of 303.2 K. The mass flow rate ratios for water/ethylene glycol to LNG are 12.5, 8.3, 6.3, and 5. The data indicate a clear correlation between an increase in LNG mass flow rate and a decrease in NG outlet temperature, with values dropping from the range of 284.0 K–286.6 K to 265.0 K–271.5 K.

To summarise, the characteristics of NG, including density, viscosity, heat capacity, and thermal conductivity, demonstrate fluctuations in response to temperature when it is in the compressible fluid phase, which encompasses both the compressible liquid and supercritical states. The velocity and temperature distributions of NG within the plate heat exchanger are subject to various factors, including but not limited to the number of channels, inlet temperature of water/EG, and mass flow rate ratios of LNG to water/EG. These factors have a significant impact on the aforementioned distributions. The empirical evidence suggests that the operational span of LNG in the heat exchanger is broader above the critical point than below it, irrespective of the absence of any phase transition in the LNG. The extended scope of this range permits the outlet temperatures of NG to surpass 273.2 K. In order to attain a homogeneous NG outlet temperature profile and approach an outlet temperature of 273.2 K, it is advisable to employ fewer than five channels and maintain a water/EG to LNG mass flow rate ratio greater than five.

Thus, the appropriate operational parameters for the recovery of cold energy in the corrugated plate heat exchanger utilising a water/EG mixture (with a mixing volume ratio of 7:3) can be succinctly outlined as follows: The experimental conditions involved an NG pressure range of 70–100 bar, inlet temperatures of water/EG ranging from 293.2 K to 303.2 K, an outlet temperature of water/EG above 259.2 K, a channel count of less than 5, and a mass flow rate ratio of water/EG to LNG greater than 5. The subsequent techno-energy analysis of a DCS incorporating cold energy recovery will employ these safe operational conditions.

5. Techno-Energy Analysis of the Combination of 500 MW Natural Gas-Fired Power Plant and District Cooling System (DCS) with Cold Energy Recovery

Within this section, a comparative analysis was carried out on two schemes based on Southeast Asia: (i) Scheme I, as shown in Figure 11, comprises a 500 MW power plant that uses natural gas (NG) as fuel [29], several buildings that require 0.25 MW for cooling [30], and an LNG tank that operates at a pressure of 1.3 bar and a temperature of 111.2 K [31]. (ii) Scheme II, depicted in Figure 12, includes all the components of Scheme I and additionally integrates a cold energy recovery system that operates above the critical point of NG.

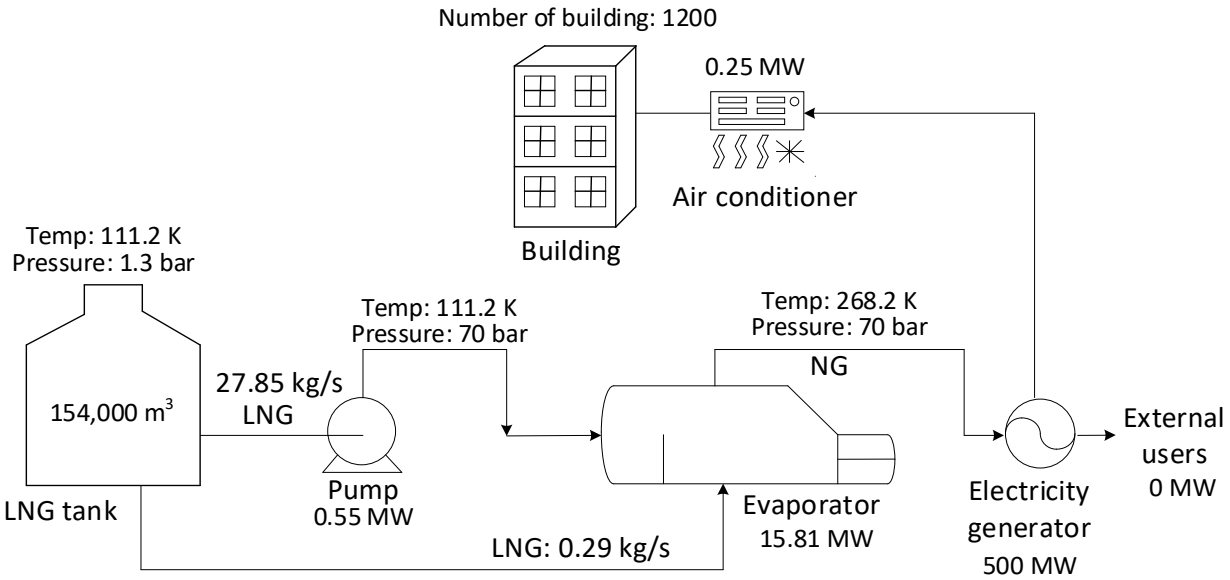

Figure 11. Current combination of natural gas-fired power plant and DCS without recovery cold energy from regasification (Scheme I).

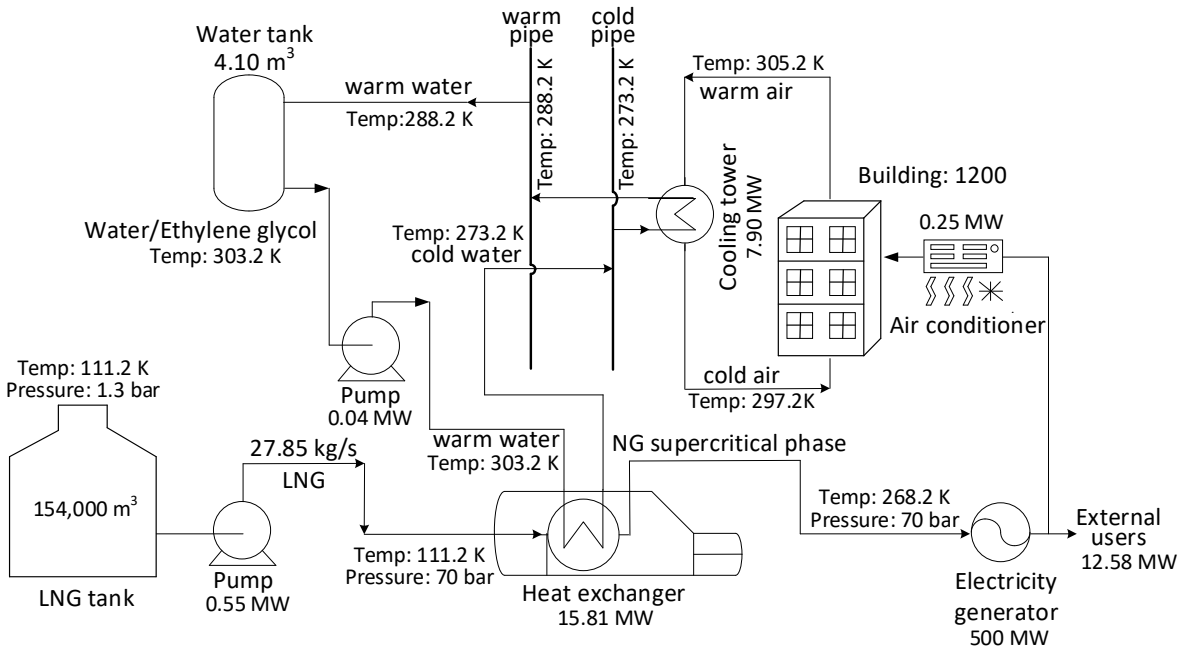

Figure 12. The proposed combination of natural gas-fired power plant, DCS, and cold energy recovery from LNG gasification above critical pressure as a compressible supercritical state (Scheme II).

5.1. Detailed Analysis for Scheme I

i. Number of buildings powered by the power plant for cooling.

The average power for each building, $P_{building\_cooling,}$ is 0.25 MW. The coefficient of performance, $COP_{building\_cooling,}$ is 0.6. The estimated number of buildings in the city, $n_{building,}$ powered by the 500 MW gas-fired power plant for cooling is 1200.

$$n_{building} = \frac{COP_{building\_cooling} P_{building\_input}}{P_{building\_cooling}} \quad (6)$$

ii. LNG required for power plant

The power plant output power is 500 MW; $\eta_{Chemical\_Mechanical}$ is 0.35; $\eta_{Mechnical\_Electricity}$ is 0.95 [32].

$$P_{combustion} = \frac{P_{powerplant}}{\eta_{Chemical\_Mechanical}\eta_{Mechanical\_Electricity}} \quad (7)$$

The combustion heat, $H_{combustion\_NG}$ is 54 MJ/kg [33]. The mass flow rate m_{NG} is

$$m_{NG} = \frac{P_{combustion}}{H_{comubstion\_NG}} \quad (8)$$

The mass flow rate for the power plant, m_{NG} is 27.85 kg/s.

iii. LNG required for regasification

The power for regasification, $P_{regasification}$ is 15.81 MW, which is the same as in Scheme II. The LNG mass flow rate, m_{NG_gas}, for regasification is 0.29 kg/s.

iv. Pump for LNG

The pressure difference of LNG before and after the pump is 1.3 bar and 70 bar, respectively. The pump hydraulic efficiency is 0.75. The density of LNG is 468 kg/m^3. The power for the pump, $P_{pump,}$ is

$$P_{pump} = \frac{V_{LNG}(p_{LNG\_2} - p_{LNG\_1})}{\eta_{pump}} \quad (9)$$

$$V_{LNG} = \frac{m_{LNG}}{\rho_{LNG}} \tag{10}$$

Through calculation, P_{pump} is 0.55 MW.

v. Size of the LNG tank

The time for LNG storage is 30 days. The storage tank size is

$$V_{storage\_tank} = 30 \times 24 \times 3600 \times V_{LNG} \tag{11}$$

The storage tank size is 154,000 m^3. This is reasonable in comparison with the literature [1].

5.2. Detailed Analysis for Scheme II

i. Plate heat exchanger

The mass flow rate for water/EG is given in Equation (12).

$$m_{water} = 5m_{LNG} \tag{12}$$

The temperatures of water/EG before and after the heat exchanger are 303.2 K and 273.2 K, respectively. The temperatures of LNG before and after the heat exchanger are 111.2 K and 268.2 K, respectively.

The power for the plate heat exchanger

$$Pc_{plate\_heat\_exchange} = m_{water}C_{p\_water}(T_{water\_1} - T_{water\_2}) \tag{13}$$

The power for the plate heat exchanger, $Pc_{plate\_heat\_exchange}$, is 15.81 MW.

ii. Cooling tower

The water/EG temperatures before and after the cooling tower are 288.2 K and 273.2 K, respectively.

$$Pc_{cooling\_tower} = m_{water}C_{p\_water}(T_{water\_3} - T_{water\_2}) \tag{14}$$

The power for the cooling tower is 7.90 MW.

iii. Pump for water/EG

The pressure loss for the pipe network [2] is

$$\Delta p_{water} = \frac{\lambda_{pipe}}{d_{pipe}} \frac{L_{pipe}}{2} \rho_{water} {u_{water}}^2 \tag{15}$$

Here, the pipe diameter, $d_{pipe,}$ is set as 250 mm; the friction factor, $\lambda_{pipe,}$ is 0.0156; the length of the pipe, $L_{pipe,}$ is 1000 m. The velocity of water, $u_{water,}$ is 2.75 m/s. Then, the pressure loss in the pipe network is 2.43×10^5 Pa. The volume flow rate is 0.13 m^3/s. If the pump conversion efficiency is 79% [2] and the pressure loss in the regasification heat exchanger is omitted, then the pump power for the water is 0.04 MW.

iv. Size of water tank

The equation for water energy storage [34] is

$$Q = m_{water}C_{p\_water}V_{water\_tank}\Delta T_{water} \tag{16}$$

The storage capacity for water is about 9 kWh/m^3 [35], so the size of the water tank is 4.10 m^3.

v. Power for external users

The equation for calculating the outlet power for external users is

$$Pc_{elec\_output} = P_{powerplant} - P_{pump} - P_{building_{input}} + Pc_{cooling\_tower} \quad (17)$$

The power for external users, Pc_{elec_output} is 12.58 MW. Therefore, the total saved power of Scheme II in comparison with Scheme I is 28.39 MW since the energy needed for regasification in Scheme I is 15.81 MW, and, thus, is saved. Hence, within the safe operating parameters of LNG cold recovery utilising a corrugated heat exchanger, there is a recovery of 28.39 MW/15.81 MW or a 180% saving in regasification consumption.

Finally, it can be seen that the LNG cold energy recovery above the LNG critical point can improve energy utilisation efficiency significantly.

6. Conclusions

The primary objective of this study is to assess the viability of utilising LNG cold energy recovery within a district cooling system. Following this, a techno-energy analysis is performed to examine the amalgamation of a 500 MW gas-fired power plant and a DCS in two distinct scenarios: one without cold energy recovery (Scheme I) and the other with cold energy recovery (Scheme II). Based on the available evidence, the conclusions are drawn as follows:

i. The simulation of heat transfer in the corrugated plate heat exchanger is executed through the utilisation of a 2D model in COMSOL 5.2a. The k-ω model is utilised in the turbulent flow module to simulate the fluid flow, whereas the heat transfer module is responsible for forecasting the fluid outlet temperature and heat flux. The process of validating the CFD model involves a comparison of its outcomes with experimental data obtained from a system comprising LN and water. The simulation results demonstrate the crucial significance of the gas film adhered to the channel wall in impacting the heat transfer process between LN and water within the corrugated plate heat exchanger. The efficacy of the constructed models is exemplified by a mere 2.3% margin of error.

ii. The examination of the methane phase diagram reveals that LNG has the potential to engage in thermal interaction with water/EG in two distinct scenarios: when operating below the critical point, specifically at 10 bar, and when operating above the critical point, within the range of 70 to 100 bar.

iii. The CFD models that have been validated are utilised to assess the thermal efficiency of the corrugated plate heat exchanger when using LNG and water/EG. LNG is commonly regarded as a fluid with negligible compressibility. The operational range for LNG below its critical point is restricted to avoid the solidification of water and ethylene glycol and the vaporisation of LNG. The customary ratio of mass flow rate between LNG and water/EG is 3:1, which leads to a temperature increase of 10–20 K at the outlet of LNG in comparison to its inlet temperature.

iv. Additionally, simulations are performed to examine the heat transfer phenomenon between LNG and water/EG above the critical point while taking into account natural gas (NG) as a compressible fluid. The findings indicate that the temperature of the NG outlet can attain a value of around 273.2 K under the condition that the temperature of the LNG inlet is 111.2 K. The present study conducts an analysis of the influencing parameters, namely the number of channels, water/EG inlet temperature, water/EG mass flow rate, and LNG mass flow rate. The attainment of optimal performance is realised by utilising no more than five channels and maintaining a minimal ratio of flow rate between water/EG and LNG.

v. Ultimately, the utilisation of a corrugated plate heat exchanger is implemented to facilitate the recuperation of cold energy between liquefied natural gas and water/ethylene glycol. The study conducted a techno-energy analysis of the integration of a 500 MW gas-fired power plant and DCS. The findings indicate that the inclusion of LNG cold energy recovery above the NG critical point leads to a significant reduction of 180%

in regasification consumption compared to the combination without cold energy recovery.

7. Future Works

While this study has made significant strides in understanding the heat transfer mechanisms involved in LNG cold energy recovery, it is essential to acknowledge its limitations and potential future works.

The current study leans on simplified assumptions, particularly in considering constant material properties for LNG below the critical point. Future research should aim to employ more sophisticated material property models that account for a wider range of temperature and pressure conditions, as real-world applications often involve dynamic variations in these parameters. The exact mechanism responsible for the formation of the gas film along the channel walls, a critical factor in heat transfer, is not extensively explored in this study. Future research should explore deeper into the causes and dynamics of gas film formation to enhance our understanding and optimise its influence on heat exchange.

Although this study has primarily focused on feasibility analysis, the next step should involve a more in-depth economic analysis. This could include conducting cost-benefit analyses, assessing lifecycle costs, and performing sensitivity analyses to determine the economic viability of implementing LNG cold energy recovery in practical applications.

In future research endeavours, the integration of artificial intelligence (AI) can potentially revolutionise the optimisation of energy systems. One pivotal area is the development of AI algorithms that continuously optimise power and cooling supply operation to the DCS with LNG cold recovery in real time. These algorithms could dynamically adjust parameters like mass flow rates, temperatures, and pressure settings, thereby maximising energy efficiency and cost-effectiveness.

Author Contributions: Y.L.: Experiment, Investigation, Writing Original Draft and Revision. X.L.: Simulation, Validation, Data Analysis, Investigation, Writing Original Draft. Y.C.: Investigation and Writing Revision. J.A.: Conceptualisation, Methodology. M.M.-V.: Supervision. All authors have read and agreed to the published version of the manuscript.

Funding: The authors would like to acknowledge the financial support provided by the Newton Fund Malaysia-UK Research and Innovation Bridges Programme by the Engineering and Physical Sciences Research Council (EPSRC) UK with grant reference EP/P015379/1. Yang Luo acknowledges the Research Development Grant RDF/21/01-028 funded by Xi'an Jiaotong-Liverpool University. Yi Chen acknowledges the Research Development Grant RDF/21/02-019 funded by Xi'an Jiaotong-Liverpool University.

Data Availability Statement: Not Applicable.

Conflicts of Interest: The authors declare no conflict of interest.

Nomenclature

b	amplitude of corrugation, m
C_p	heat capacity, J/(kg·K)
C_{p_NG}	heat capacity of natural gas, J/(kg·K)
$C_{p\_seawater}$	heat capacity of seawater, J/(kg·K)
$COP_{building\_cooling}$	building air conditioner coefficient of performance
d_h	hydraulic diameter, m
d_{pipe}	diameter of water pipe, m
h	convective heat transfer coefficient, W/(m^2·K)
$H_{combustion\_NG}$	combustion heat of natural gas, J/kg
k	thermal conductivity, W/(m·K)
L_{pipe}	length of water pipe network, m
m_{LNG}	mass flow rate of liquefied natural gas, kg/s
m_{NG}	mass flow rate of natural gas, kg/s
$m_{seawater}$	mass flow rate of seawater, kg/s
$n_{building}$	number of buildings
Nu	Nusselt number
p	pressure, Pa
p_{LNG}	pressure of liquefied natural gas, Pa
p_{water}	pressure loss in the water pipe, Pa
$Pc_{cooling\_tower}$	power of cooling tower in Scheme II, W
Pc_{elec_output}	electricity output power in Scheme II, W
$Pc_{plate\_heat\_exchange}$	power of plate heat exchanger in Scheme II, W
$P_{building\_cooling}$	power for building cooling, W
$P_{building\_input}$	input power for building cooling, W
$P_{combustion}$	power of combustion, W
P_{elec_output}	electricity output power in Scheme I, W
$P_{powerplant}$	power of gas-fired power plant, W
P_{pump}	power of pump, W
$P_{regasification}$	power of regasification, W
q	heat flux, W/m^2
Q	heat source, W/m^3
Re	Reynolds number
S	Strain rate tensor, Pa
T	temperature, K
T_{in}	fluid inlet temperature, K
T_{NG}	temperature of natural gas, K+
$T_{seawater}$	temperature of seawater, K
u	velocity, m/s
u_{water}	water velocity, m/s
U	mass flow rate, kg/s
V_{LNG}	volume flow rate, m^3/s
$V_{storage\_tank}$	volume of storage tank, m^3
V_{water_tank}	volume of water tank, m^3
Greek	
γ	aspect ratio of chevron corrugation
η	enlargement factor of corrugation surface
$\eta_{Chemical\_Mechanical}$	efficiency of chemical energy conversion to mechanical energy
$\eta_{Mechanical\_Electricity}$	efficiency of mechanical energy conversion to electrical energy
η_{pump}	pump efficiency
λ	corrugation pitch, m
λ_{pipe}	friction factor for water pipe
μ	dynamic viscosity, Pa·s
μ_T	turbulent viscosity, Pa·s
ρ	density, kg/m^3
ρ_{LNG}	density of liquefied natural gas, kg/m^3
τ	viscous stress tensor, Pa
Abbreviation	
DCS	district cooling system
EG	ethylene glycol
LN	liquid nitrogen
LNG	liquefied natural gas
NG	natural gas

References

1. Amin, M.; Majid, A.; Ya, H.H.; Mamat, O.; Mahadzir, S. Techno Economic Evaluation of Cold Energy from Malaysian Liquefied Natural Gas Regasification Terminals. *Energies* **2019**, *12*, 4475. [CrossRef]
2. Antonio, M.; Ojeda, C. District Cooling in Lima, Peru—Identification of Potentials and Barriers for Developing District Cooling in San Isidro Financial District. Master's Thesis, Aalborg University, Aalborg, Denmark, 2017.
3. Arachchige, U.; Mohsin, M.; Melaaen, M.C. Optimized Carbon Dioxide Removal Model for Gas Fired Power Plant. *Eur J. Sci. Res.* **2012**, *86*, 348–359.

4. Atienza-márquez, A.; Bruno, J.C.; Coronas, A. Cold recovery from LNG-regasification for polygeneration applications. *Appl. Therm. Eng.* **2018**, *132*, 463–478. [CrossRef]
5. Foss, M.M. *Introduction to LNG an Overview on Liquefied Natural Gas (LNG), Its Properties, the LNG Industry, and Safety Considerations*; Center for Energy Economics Consultancy Report; The University of Texas: Austin, TX, USA, 2012.
6. Cheng, H.; Ju, Y.; Fu, Y. Thermal performance calculation with heat transfer correlations and numerical simulation analysis for typical LNG open rack vaporiser. *Appl. Therm. Eng.* **2019**, *149*, 1069–1079. [CrossRef]
7. Chu, T. Research on the Potential of District Cooling and Energy Savings in Wuhan, China. Master's Thesis, Institute of Applied Physics and Electronics, Umeå University, Umeå, Sweden, 2008.
8. Davis, L.W.; Gertler, P.J. Contribution of air conditioning adoption to future energy use under global warming. *Proc. Natl. Acad. Sci. USA* **2015**, *112*, 5962–5967. [CrossRef]
9. Dong, Y.; Coleman, M.; Miller, S.A. Greenhouse Gas Emissions from Air Conditioning and Refrigeration Service Expansion in Developing Countries. *Annu. Rev. Environ. Resour.* **2021**, *46*, 59–83. [CrossRef]
10. Egashira, S. LNG Vaporizer for LNG Regasification Terminal. *KOBELCO Technol. Rev.* **2013**, *32*, 64–69.
11. Erdogmus, B.; Toksoy, M.; Ozerdem, B.; Aksoy, N. Economic assessment of geothermal district heating systems: A case study of Balcova–Narlidere, Turkey. *Energy Build.* **2006**, *38*, 1053–1059. [CrossRef]
12. Eveloy, V.; Ayou, D.S. Challenges, and Future Opportunities, with Emphasis on Cooling-Dominated Regions. *Energies* **2019**, *12*, 235. [CrossRef]
13. Gürel, B. Thermal performance evaluation for solidification process of latent heat thermal energy storage in a corrugated plate heat exchanger. *Appl. Therm. Eng.* **2020**, *174*, 115312. [CrossRef]
14. Han, D.; Xu, Q.; Zhou, D.; Yin, J. Design of heat transfer in submerged combustion vaporiser. *J. Nat. Gas Sci. Eng.* **2016**, *31*, 76–85. [CrossRef]
15. Hassan, J. Next Generation District Cooling Network—A High-Level Overview. Clean Cooling. In Proceedings of the New "Frontier Market" for UAE & GCC Region, Dubai, United Arab Emirates, 9–10 April 2018; pp. 9–10.
16. International Energy Agency. *The Future of Cooling—Opportunities for Energy-Efficient Air Conditioning*; IEA: Paris, France, 2018; Available online: https://www.iea.org/reports/the-future-of-cooling (accessed on 6 August 2023).
17. International Energy Agency. *The Future of Cooling in Southeast Asia*; IEA: Paris, France, 2019; Available online: https://www.iea.org/reports/the-future-of-cooling-in-southeast-asia (accessed on 6 August 2023).
18. International Gas Union. *World Gas LNG 2022 Report*; IGU: Barcelona, Spain, 2022; Available online: https://www.igu.org/resources/world-lng-report-2022/ (accessed on 6 August 2023).
19. Inayat, A.; Raza, M. District cooling system via renewable energy sources: A review. *Renew. Sustain. Energy Rev.* **2020**, *107*, 360–373. [CrossRef]
20. Invernizzi, C.M.; Iora, P. The exploitation of the physical exergy of liquid natural gas by closed power thermodynamic cycles. An overview. *Energy* **2016**, *105*, 2–15. [CrossRef]
21. Keçebas, A. Energetic, exergetic, economic and environmental evaluations of geothermal district heating systems: An application. *Energy Convers. Manag.* **2015**, *65*, 546–556. [CrossRef]
22. Koku, O.; Perry, S.; Kim, J. Techno-economic evaluation for the heat integration of vaporisation cold energy in natural gas processing. *Appl. Energy* **2014**, *114*, 250–261. [CrossRef]
23. Lee, I.; You, F. Systems design and analysis of liquid air energy storage from liquefied natural gas cold energy. *Appl. Energy* **2019**, *242*, 168–180. [CrossRef]
24. Li, S.; Ju, Y. Review of the LNG intermediate fluid vaporiser and its heat transfer characteristics. *Front. Energy* **2022**, *16*, 429–444. [CrossRef]
25. Liu, W.; Hashim, H.; Lim, J.S.; Zarina, A.M.; Liew, P.Y.; Ho, W.S. Technical and Economic Evaluation of District Cooling System as Low Carbon Alternative in Kuala Lumpur City Technical and Economic Evaluation of District Cooling System as Low Carbon Alternative in Kuala Lumpur City. *Chem. Eng. Trans.* **2017**, *56*, 529–534. [CrossRef]
26. Looney, C.M.; Oney, S.K. Seawater District Cooling and Lake Source District Cooling. *Energy Eng.* **2007**, *104*, 34–45. [CrossRef]
27. Zhao, Z.; Zhou, Y.; Ma, X.; Chen, X.; Li, S.; Yang, S. Numerical Study on Thermal Hydraulic Performance of Supercritical LNG in Zigzag-Type Channel PCHEs. *Energies* **2019**, *12*, 548. [CrossRef]
28. Neyer, D.; Ostheimer, M.; Dipasquale, C.; Köll, R. Technical and economic assessment of solar heating and cooling—Methodology and examples of IEA SHC Task 53. *Sol. Energy* **2018**, *172*, 90–101. [CrossRef]
29. Arachchige, U.; Melaaen, M. Aspen Plus Simulation of CO2 Removal from Coal and Gas Fired Power Plants. *Energy Procedia* **2012**, *23*, 391–399. [CrossRef]
30. Popovski, E.; Fleiter, T.; Santos, H.; Leal, V.; Oliveira, E. Technical and economic feasibility of sustainable heating and cooling supply options in southern European municipalities-A case study for Matosinhos, Portugal. *Energy* **2018**, *153*, 311–323. [CrossRef]
31. Qi, C.; Wang, W.; Wang, B.; Kuang, Y.; Xu, J. Performance analysis of submerged combustion vaporiser. *J. Nat. Gas Sci. Eng.* **2016**, *31*, 313–319. [CrossRef]
32. Sand, J.R.; Fischer, S.K.; Baxter, V.D. *Energy and Global Warming Impacts of HFC Refrigerants and Emerging Technologies: TEWI-III*; Oak Ridge National Laboratory: Oak Ridge, TN, USA, 1997.

33. Tiantian, Z.; Yufei, T.; Li, B. Numerical simulation of a new district cooling system in cogeneration plants. *Energy Procedia* **2012**, *14*, 855–860. [CrossRef]
34. Wu, T.; Cao, B.; Zhu, Y. A field study on thermal comfort and air-conditioning energy use in an office building in Guangzhou. *Energy Build.* **2018**, *168*, 428–437. [CrossRef]
35. Zhen, L.; Lin, D.M.; Shu, H.W.; Jiang, S.; Zhu, Y.X. District cooling and heating with seawater as heat source and sink in Dalian, China. *Renew. Energy* **2007**, *32*, 2603–2616. [CrossRef]